Hindawi
Journal of Nanomaterials
Volume 2019, Article ID 3242136, 9 pages
https://doi.org/10.1155/2019/3242136

Research Article

Templated Fabrication of Graphitic Carbon Nitride with Ordered Mesoporous Nanostructures for High-Efficient Photocatalytic Bacterial Inactivation under Visible Light Irradiation

Jianqin Chen,[1,2] Wenting Lin,[1] Liyan Xie,[1,2] Jianhui Huang,[1,3] and Wanjun Wang[4]

[1]*College of Environmental and Biological Engineering, Putian University, Putian 351100, China*
[2]*Key Laboratory of Ecological Environment and Information Atlas, Fujian Provincial University, Putian University, Putian 351100, China*
[3]*Fujian Provincial Key Laboratory of Ecology-Toxicological Effects and Control for Emerging Contaminants, Putian University, Putian 351100, China*
[4]*Institute of Environmental Health and Pollution Control, School of Environmental Science and Engineering, Guangdong University of Technology, Guangzhou, 510006 Guangdong, China*

Correspondence should be addressed to Jianhui Huang; owenhuang95@163.com and Wanjun Wang; wanjun_w@163.com

Received 30 January 2019; Accepted 21 May 2019; Published 3 June 2019

Academic Editor: P. Davide Cozzoli

Biohazards are widely present in water, and a variety of waterborne diseases can be aroused by contaminated water. Therefore, the effective removal of biological hazards from water is necessary for the protection of human health. In this study, graphitic carbon nitride (g-C_3N_4) with ordered mesoporous nanostructures was successfully synthesized by a template method using SBA-15 as a hard template. The morphology, crystal structure, specific surface area, molecular structure, and light absorption properties of the as-prepared sample were characterized by TEM, XRD, BET, FT-IR, and UV-Vis DRS, respectively. The photocatalytic performance of the ordered mesoporous g-C_3N_4 was evaluated by the inactivation of *Escherichia coli* K-12 in water under visible light irradiation. Results showed that the bacterial inactivation efficiency can reach as high as 99% within 2 h of VL irradiation, which is 4 times higher than that of bulk g-C_3N_4. Moreover, the photocatalytic bacterial inactivation mechanism was revealed by a scavenging study, and the main active species in the photocatalytic inactivation process was found to be a photogenerated hole. This work will provide useful information for the development of new efficient g-C_3N_4-based materials for enhanced water disinfection applications by introducing ordered mesoporous nanostructures in a photocatalyst design and fabrication.

1. Introduction

Water is indeed the most essential substance for the life of all beings. It is of major importance to human civilization and at the core of sustainable development. Due to a variety of environmental pollutions, the drinking water which contains a lot of bacteria and viruses could seriously affect people's health [1–3]. It was reported that 750 million people still lack access to improved drinking water sources (WHO, 2015). The consequences are daunting; for example, only diarrhea kills about 2.2 million people every year; most of them are the children under the age of 5 [4]. Ensuring reliable access to clean and affordable water is considered one of the most basic humanitarian goals and remains a great challenge. Therefore, it is necessary to carry out comprehensive disinfection of drinking water. At present, chlorination is the most common disinfection technology, but it easily leads to "carcinogenic, teratogenic, mutagenic" problems [5, 6]. Therefore, it is urgent to develop highly efficient, environmentally friendly, and economical disinfection technology without producing disinfection by-products. Photocatalytic technology combines the advantages of this series. In the photocatalytic process, photogenerated electrons, holes, and their active species can destroy the structure of various

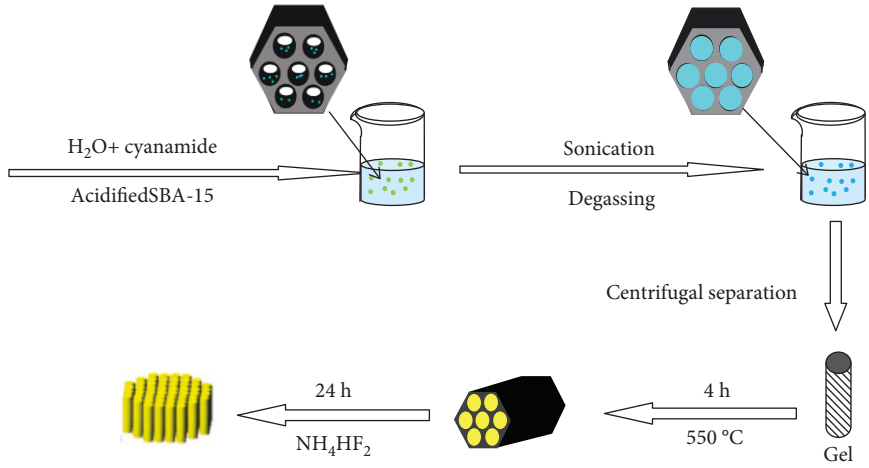

Figure 1: Schematic illustration of the synthesis process for the ordered mesoporous g-C_3N_4.

pathogens and their components with strong redox ability, which greatly improves the efficiency of disinfection [7]. At the same time, it can also degrade the toxic complex released during the disinfection process and remove the by-products caused by traditional chlorinated disinfection. Hence, the photocatalytic disinfection technology has a wide range of application prospects.

For the successful application of photocatalytic disinfection technology, the development of cost-effective photocatalysts has been the central mission. Over the past several decades, TiO_2 has been extensively studied as an effective, reusable, and sustainable photocatalyst for bacterial inactivation. However, TiO_2 can only be activated by UV light ($\lambda < 400$ nm), which is only about 4% of the solar spectrum. Thus, solar energy cannot be utilized efficiently for photocatalytic disinfection. Consequently, considerable efforts have been devoted into developing new visible-light-driven (VL) photocatalysts, which have been evolved from modified TiO_2 [8–12] to non-TiO_2-based semiconductor materials, such as metal oxides [13], sulfides [14], or oxynitrides [15]. Nevertheless, it is still of great challenges to develop new photocatalysts which are required to be efficient, stable, economic, and especially capable of working under visible or even near-infrared light. Recently, nonmetallic polymer semiconductor graphitic carbon nitride (g-C_3N_4) has gained intense interests due to excellent properties in thermal and chemical stability and easy to control the structural properties. In particular, g-C_3N_4 has a narrow band gap (2.7 eV), which has good responsiveness to visible light (absorbable wavelengths less than 460 nm) and therefore shows great potential in various photocatalytic applications [16–18].

Recently, a series of studies have shown that g-C_3N_4 exhibits high photocatalytic activity for bacterial inactivation applications [19, 20]. Our previous work has also shown that the g-C_3N_4 with a mesoporous structure could inactivate 2.5×10^6 cfu/mL of *E. coli* cells within 4 h under VL irradiation [21]. However, the photocatalytic disinfection activities of g-C_3N_4 are seriously limited by inherent defects originating from the π-conjugated system. In addition, the bulk g-C_3N_4 with a low specific surface area and a poor pore structure usually leads to a less-active site and a fast-charge recombination rate [22]. Hence, it is urgent to modify g-C_3N_4 with optimized morphology and textural, electronic, and optical properties to promote photocatalytic efficiency. Among various carbon nitride materials, an ordered mesoporous structure endows the materials with a high specific surface area and pore structures which has already been demonstrated as a successful way to enhance charge separation efficiency, as well as the mass diffusion/transfer during photocatalytic reactions. Therefore, it can greatly enhance the photocatalytic performance of semiconductor materials [23–26] including the organic pollutant degradation. Herein, we report the preparation of the ordered mesoporous g-C_3N_4 (omg-C_3N_4), with mesoporous silica SBA-15 as the hard template. The obtained omg-C_3N_4 was used for photocatalytic inactivation of *E. coli* K-12 cells for the first time. The photocatalytic bacterial inactivation mechanisms were also investigated in detail.

2. Experimental Section

2.1. Preparation of Mesoporous Molecular Sieve SBA-15. SBA-15 was prepared according to the procedure reported by Zhao et al. [27]. In a typical synthesis, 2 g P123 (polyethylene oxide-polypropylene oxide-polyethylene oxide triblock copolymer) was added to 2 mol/L HCl solution (75 mL); after stirring for 2 h, 4.55 mL of ethyl orthosilicate (TEOS) was added and stirred at 40°C for 24 hours. The above mixture was then charged into an autoclave, heated at 100°C for 24 hours. The resulting solution was centrifuged, washed, and dried at room temperature. The final white product was calcined at 550°C for 4 hours with a heating rate of 1°C min^{-1}.

2.2. Preparation of omg-C_3N_4. As is shown in Figure 1, 1.5 g SBA-15 was added into 1.0 mol/L HCl solution (20 mL) and acidified at 80°C for 6 hours. And then the white precipitate was centrifuged and dried. The treated silica template was impregnated in 22.5 g water solution containing 8 g of cyanamide (Sigma-Aldrich, 99%). The mixture was stirred for

1 h under sonication and reduced pressure. The obtained mixture was centrifuged, dried in air, and finally calcined at 550°C for 4 h at a heating rate of 2.3°C min^{-1}. The resulting powder was treated with ammonium bifluoride (NH_4HF_2, 4 M) for 24 h to remove the silica, followed by filtration, washing with water and ethanol 4 times and drying at 80°C under vacuum condition.

2.3. Preparation of Bulk-g-C_3N_4. 5.0 g cyanamide was placed in a crucible, calcined at 520°C for 4 h, and the rate of heating was 2.3°C/min to obtain bulk *g*-C_3N_4 (B-C_3N_4).

2.4. Characterization. The general morphologies of the products were characterized by scanning electron microscopy (FESEM, FEI, Quanta 400 FEG). Transmission electron microscopy (TEM) was recorded on a FEI Tecnai 20 microscope. The surface area of the catalyst was measured by Micromeritics' ASAP 2020 fully automated physical chemical adsorption apparatus. The samples were degassed under vacuum at 160°C for 6 h and then measured at liquid nitrogen temperature (77 K). The method of measurement is a static method, according to the adsorption isotherm, using the multipoint BET method to calculate the specific surface area. The crystal structures of the synthesized materials were determined using X-ray diffractometry (Labx XRD-6000, Shimadzu, Japan) with Cu Kα radiation (wavelength λ = 0.15418 nm) at a scanning rate of 0.05°, at 2θ/s, and the scanning range was 10–60°. UV-Vis diffuse reflection spectroscopy (DRS) was performed on a Varian Cary 100 Scan UV-visible system with $BaSO_4$ as the reference material. The structure of prepared materials was characterized by a Fourier transform infrared spectrometer (TENSOR II, Bruker). Electrochemical properties were measured with a BAS Epsilon Electrochemical System, using a Pt plate as the counter electrode and an Ag/AgCl electrode (3 mol/L KCl) as the reference electrode. The ITO glass-coated samples were used as the working electrode. Photoluminescence spectra (PL) of the samples were obtained using a fluorescence spectrometer (Edinburgh FS5) with a Xe lamp as the excitation source.

2.5. Photocatalytic Performance. The photocatalytic disinfection efficiency was carried out using a xenon lamp with an operating current of 10 A (PLS-SXE-300, Beijing Perfect Light Co. Ltd.) as the light source. The light was passed through a UV and an IR cut off filter (400 nm $\leq \lambda \leq$ 700 nm). All the experimental apparatuses used in the testing were autoclaved at 121°C for 20 min to ensure sterility. The *E. coli K-12*, one of the most common bacteria, was used as model microbe to evaluate the photocatalytic inactivated performance. The bacterial cells were incubated in nutrient broth solution at 37°C for 16 h with shaking, and then, the nutrient solution was centrifuged to obtain bacterial pellet, which was washed with sterilized 0.9% saline solution, and then diluted to the desired concentration. The reaction mixture suspension containing a photocatalyst (0.1 g) and washed bacterial cells was stirred with a magnetic stirrer throughout the experiment, and the reaction temperature was maintained at 30°C. Before and after the photocatalytic disinfection treatment, 0.1 mL reaction solution was sampled and immediately diluted with sterilized saline and then spread on nutrient agar which would be incubated at 37°C for 16 h. The number of colonies formed was counted to determine the number of viable cells. All the treatment and control experiments were performed in triplicates.

2.6. Fluorescence Spectroscopy. The *E. coli K-12* before and after photocatalytic treatment were fluorescently stained with the dyes of a bacterial viability kit (gms60041.1, Molecular Probes, Shanghai Genmed Scientifics Inc.) according to procedures reported in the literature [28]. After being incubated at 25°C in the dark for 20 min, the fluorescence of samples was measured with a fluorescence microscope (Leica DMi8).

3. Results and Discussion

3.1. TEM and SEM Analyses. The textural structure of as-prepared omg-C_3N_4 was investigated using SEM and TEM. The SEM image in Figure 2(a) shows the worm-like morphology with a length of 0.4-1 μm and a diameter of 200-300 nm. The TEM image in Figure 2(b) of the omg-C_3N_4 also reveals the worm-like morphology of omg-C_3N_4. Figure 2(c) clearly displays a hexagonal arrangement of the mesopores which were typically observed in images of SBA-15 template. In this study, the effects of the sonication condition on the morphology of product were also investigated. Figure 2(d) shows the TEM images of the samples prepared without sonication, which exhibits a number of incontinuous tunnels indicating the collapsed pore structure. This can be explained by the insufficient cyanamide filled into the SBA-15 template during preparation without sonication treatment.

3.2. BET Surface Areas Analyses. The specific surface area and pore parameters were characterized by N_2-sorption measurements. The nitrogen adsorption desorption isotherms of omg-C_3N_4 and B-C_3N_4 are shown in Figure 3 which can be classified as typical IV isotherms, indicating mesoporous characteristics of as prepared materials. Table 1 shows that the specific surface area of omg-C_3N_4 can reach 163 m^2/g, which is about 10.8 times higher than that of B-C_3N_4 (15 m^2/g). The pore volume of omg-C_3N_4 is 0.598 cm^3/g, which is also much larger than that of B-C_3N_4 (0.06 cm^3/g). Therefore, the omg-C_3N_4 is expected to provide more active sites for surface catalytic reactions and will help to improve its photocatalytic bacterial inactivation activities [29].

3.3. XRD Analysis. The XRD was used to investigate the phase structure of the as-prepared omg-C_3N_4 samples using B-C_3N_4 as the reference sample. Figure 4 shows that a similar structure was detected in omg-C_3N_4 and B-C_3N_4. A diffraction peak appears at $2\theta = 13.10^o$, which corresponds to the (100) crystal face of *g*-C_3N_4. The crystal plane spacing $d_{(100)}$ is 0.679 nm, due to the formation of the stacking unit within the plane structure. Another weak diffraction peak appears at $2\theta = 27.3^o$, corresponding to the (002) crystal plane of *g*-C_3N_4, formed by the stacking of the aromatic ring [30]. Notably, the diffraction peak intensity of omg-C_3N_4 is much broader and weaker than

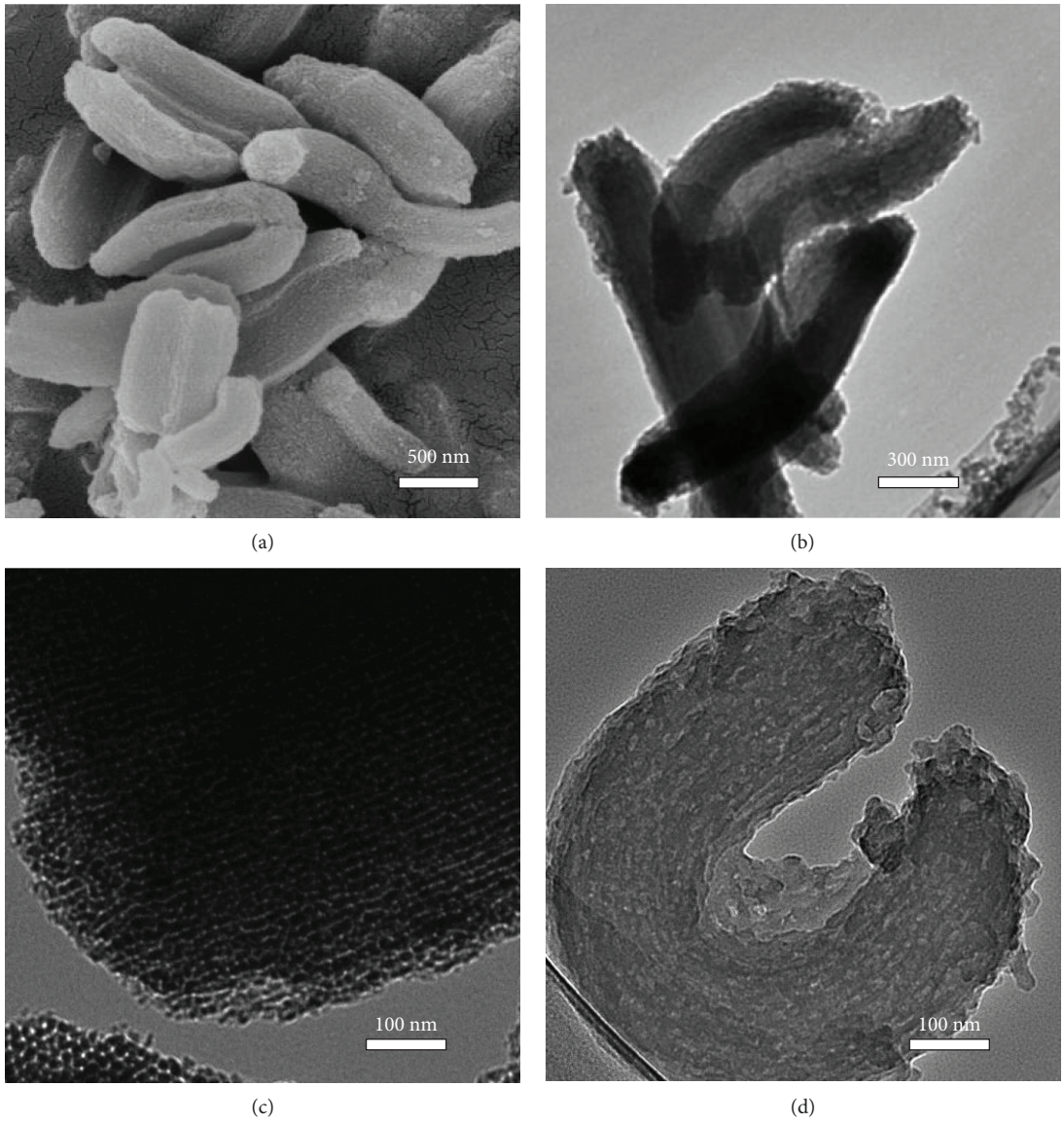

Figure 2: Scanning electron microscopy and transmission electron microscopy of prepared g-C_3N_4: (a) SEM of omg-C_3N_4, (b, c) TEM of omg-C_3N_4, and (d) TEM of sample without sonication.

that of B-C_3N_4, which indicates that the omg-C_3N_4 samples exhibited lower crystallization or smaller crystal size than the bulk sample.

3.4. Optical Property Analysis. Figure 5 shows the UV-vis absorption spectra of samples. The light absorption cut-off edge of omg-C_3N_4 is about 450 nm, while the B-C_3N_4 has a light absorption edge at 458 nm. The color of omg-C_3N_4 also shows a lighter yellow color than that of B-C_3N_4. The result indicates that the light absorption band of omg-C_3N_4 undergoes a slight blue shift which could be due to the smaller particle size of the omg-C_3N_4. Besides, Figure 5 also shows that the light absorption intensity of omg-C_3N_4 is much stronger than that of the B-C_3N_4 sample, which can be due to light reflection or transmission of scattering within the mesoporous structure of the omg-C_3N_4 network.

3.5. Photocurrent Responses of Photocatalysts. The photocurrent response of the omg-C_3N_4 electrode is shown in Figure 6 with that of B-C_3N_4 as a comparison. The photocurrent density of omg-C_3N_4 is much higher than that of B-C_3N_4, which indicates that the ordered mesostructure not only sis favorable for the interfacial separation of electron-hole pairs but also enables charge transport over longer distances. Thus, it is expected to promote antibacterial performance.

3.6. Photoluminescence Analysis. Photoluminescence (PL) emission spectroscopy was also used to measure the irradiative recombination of electrons and holes. The results in Figure 7 show that the PL emission intensity of omg-C_3N_4 is much higher than that of B-C_3N_4, indicating increased charge separation and transfer for omg-C_3N_4. This study also implies that the ordered mesoporous structure, together with

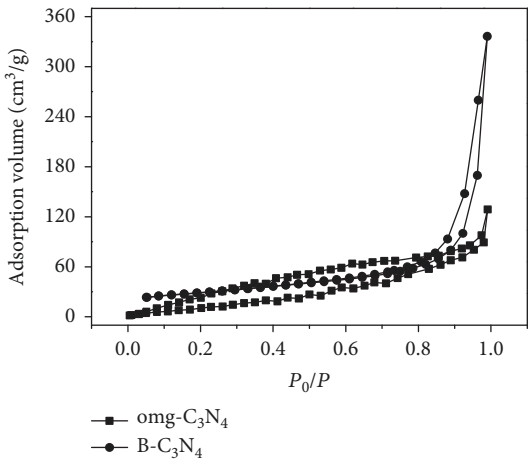

Figure 3: N_2-sorption isotherms of omg-C_3N_4 and B-C_3N_4.

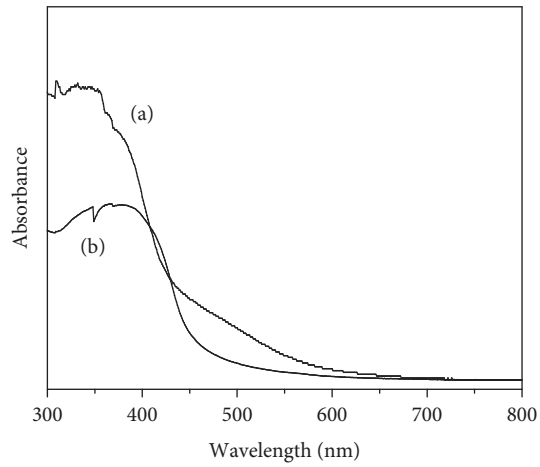

Figure 5: The UV-Vis diffuse reflectance spectra: (a) omg-C_3N_4 and (b) B-C_3N_4.

Table 1

Sample	Surface area (m^2/g)	Pore volume (cm^3/g)
omg-C_3N_4	163	0.598
B-C_3N_4	15	0.06

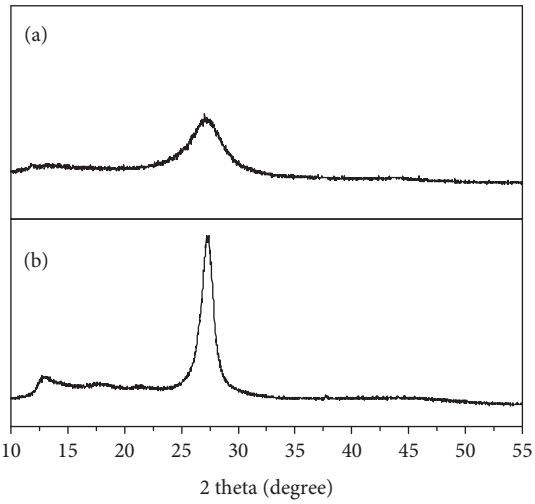

Figure 4: The X-ray diffraction pattern: (a) omg-C_3N_4 and (b) B-C_3N_4.

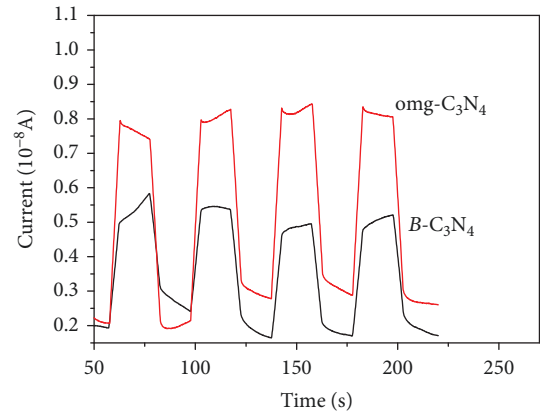

Figure 6: Photocurrent responses of omg-C_3N_4 and B-C_3N_4.

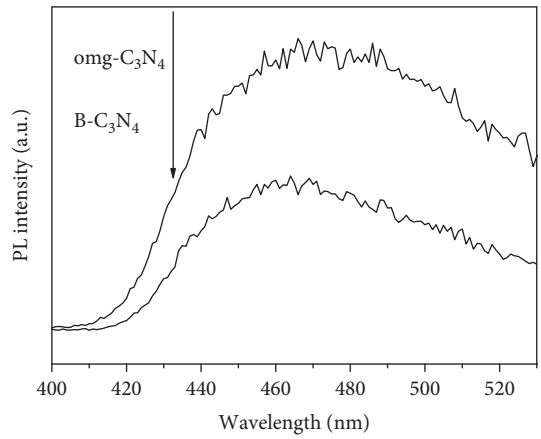

Figure 7: Photoluminescence (PL) spectra under 375 nm excitation at room temperature.

its high surface area of omg-C_3N_4, facilitates charge transfer and leads to reduced charge recombination.

3.7. IR Analysis. The molecular structure of the synthesized omg-C_3N_4 sample was analyzed by FTIR. As shown in Figure 8, the results indicate that the omg-C_3N_4 has strong peaks at 811 cm^{-1}, 1200-1800 cm^{-1}, 2180 cm^{-1}, and 3000 to 3600 cm^{-1}. The peak located at 811 cm^{-1} corresponds to the triazine ring of *g*-C_3N_4, which belongs to the absorption peak caused by the flexural vibration absorption of *g*-C_3N_4. It is the result of the agglomeration of the amino precursor in *g*-C_3N_4 after calcination at high temperature. The absorption peaks near 2180 cm^{-1} correspond to the asymmetric

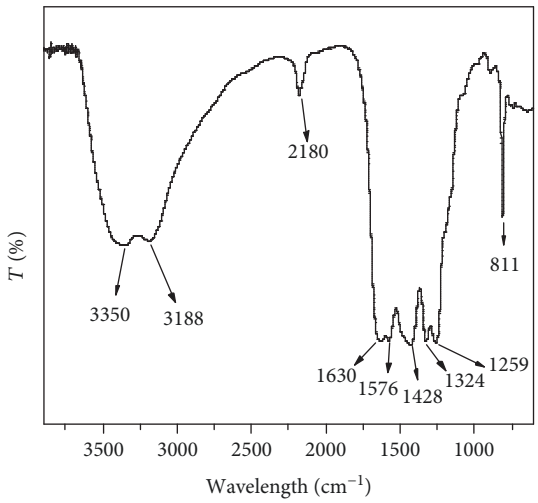

Figure 8: The FT-IR spectrum of omg-C_3N_4 and B-C_3N_4.

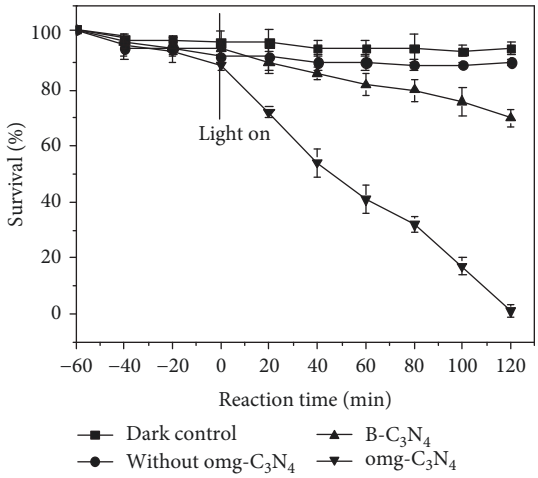

Figure 9: Photocatalytic bacterial inactivation against *E. coli* K-12 by omg-C_3N_4 and B-C_3N_4 under visible light irradiation.

stretching vibration of -C≡N bonds in *g*-C_3N_4. The broad peaks at 3188 cm^{-1} and 3350 cm^{-1} are generally symmetrical stretching vibration modes of the NH_2 and NH groups derived from incomplete condensation or residual hydrogen atoms bound to the edges of *g*-C_3N_4. In addition, the peaks at 1259 cm^{-1}, 1324 cm^{-1}, 1428 cm^{-1}, 1576 cm^{-1}, and 1630 cm^{-1} correspond to the C-N and C=N structures of *g*-C_3N_4. The overall characteristic peaks are similar to those of other graphite phases [31].

3.8. Photocatalytic Performance. Figure 9 shows the disinfection efficiency under different reaction conditions. Without light irradiation, the survival rate of bacteria remains unchanged in the presence of omg-C_3N_4 after 1 h of dark adsorption, indicating that the omg-C_3N_4 material itself is nontoxic to *E. coli* K12. In addition, the survival rate of the bacteria maintained at about 90% after 2 h of VL irradiation in the absence of omg-C_3N_4, indicating that the inactivation of bacterial by VL irradiation alone can be ignored. In the photocatalytic conditions, the survival rate of *E. coli* K12 is significantly decreased with the reaction time. When the B-C_3N_4 was used as a photocatalyst, the bacteria could be inactivated with relatively low efficiency. About 70% *E.coli* K12 still remained alive after 2 h of VL irradiation. When the omg-C_3N_4 catalyst was added, the bacterial survival rate decreased obviously. It was found that 100% *E. coli* K12 cells could be completely inactivated after 2 h of VL irradiation, indicating that omg-C_3N_4 prepared by our method has excellent photocatalytic bactericidal activity. Moreover, bacterial regrowth experiment was carried out to confirm the bacterial regrowth effect. The results showed that no detectable bacterial counts were observed even after 72 h dark incubation, indicating that the *E. coli* K-12 cells had been completely destroyed by omg-C_3N_4 rather than simply suppressing their growth or their ability to reproduce. The disinfection efficiency of omg-C_3N_4 is even much higher than that of mesoporous *g*-C_3N_4 with a considerable or much higher specific surface area [21] and the *g*-C_3N_4/BiOI-layered heterostructures [32] in our previous studies, as more than 4 h are needed to inactivate all the bacterial cells under the same reaction conditions. The enhancement can be due to the 2D accessible framework of omg-C_3N_4 which is beneficial to capture more visible light, thus significantly enhancing the bacterial inactivation efficiency.

To further confirm the photocatalytic inactivation effect of om*g*-C_3N_4, the fluorescence of untreated and photocatalytically treated *E. coli* K-12 was investigated (Figure 10). In fluorescent, the dyes used are 4′,6-diamidino-2-phenylindole (DAPI) and propidium iodide (PI), where DAPI is a semipermeable dye that allows free access to bacteria and stains live bacteria into blue. PI is a nonpermeable dye, which cannot freely enter into the bacteria and can stain dead bacteria into red. Figure 10(a) shows the bacterial cells before photocatalytic treatment exhibited intense blue fluorescence. When the catalyst is added without light irradiation, the bacterial cells still exhibit intense blue fluorescence except for a small amount of red fluorescence resulting from natural cell death, which indicates that the om*g*-C_3N_4 is nontoxic to *E. coli K-12* (Figure 10(b)). The slight red fluorescence is emitted by the om*g*-C_3N_4 catalyst. In the case of the light control experiment (without photocatalyst), the bacterial cells are also stained with blue (Figure 10(c)), indicating that the bacteria cannot be inactivated under light irradiation alone. Interestingly, the bacteria were almost dyed red in the case of om*g*-C_3N_4 with VL irradiation (Figure 10(d)), which indicates that the cell membrane is damaged, leading to the inactivation of the bacterial cells. This result is consistent with the photocatalytic inactivation experiment results in Figure 9.

3.9. Disinfection Mechanism. In order to determine the main active species during the photocatalytic inactivation process, the sodium oxalate (0.5 mmol·L^{-1}), Cr (VI) (0.05 mmol·L^{-1}), isopropanol (0.5 mmol·L^{-1}), and Fe (II)-EDTA (0.1 mmol·L^{-1}) were added to different batches of the photocatalytic reaction system with omg-C_3N_4 to capture h^+, e^-, OH·, and H_2O_2, respectively. The applied concentration

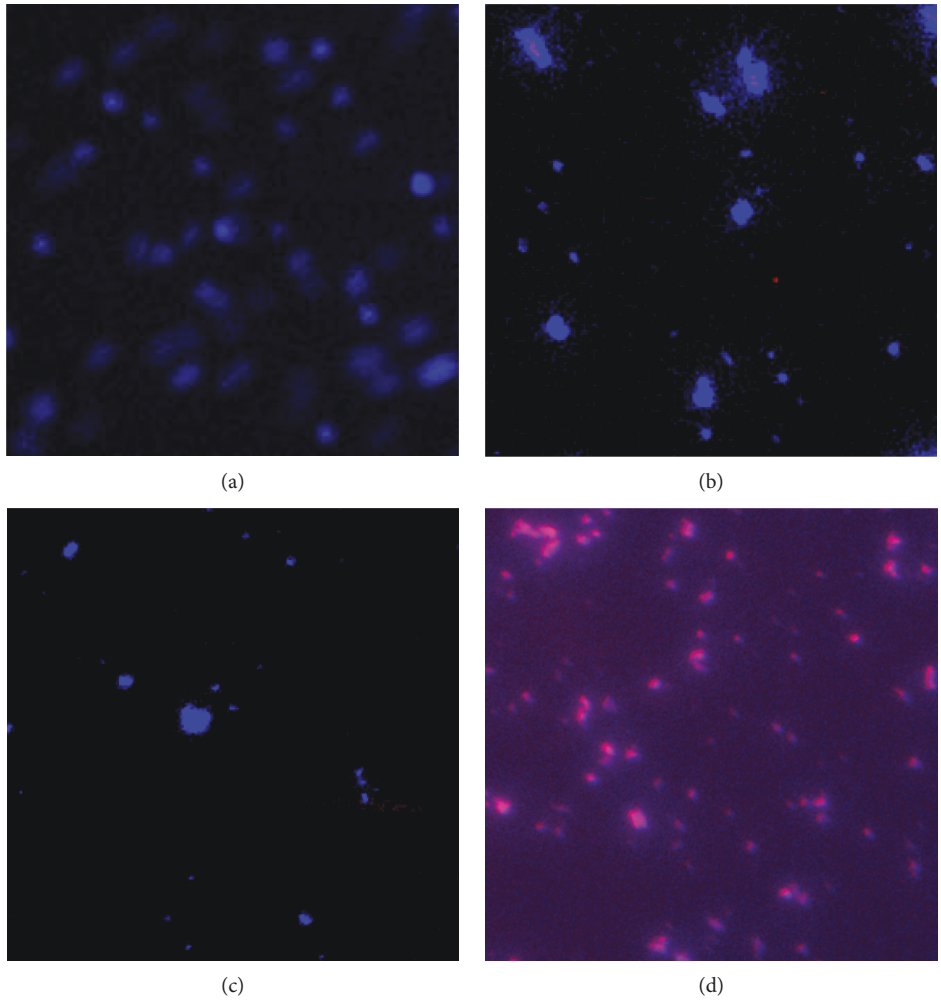

Figure 10: Fluorescence microscopic images of *E. coli* K-12 photocatalytically treated by omg-C_3N_4 under visible light irradiation: (a) blank, (b) dark control, (c) light control, and (d) after light irradiation 2 h.

of individual scavengers was optimized to ensure its maximum scavenging effect but would not cause toxicity to the bacterial cells [33]. As shown in Figure 11, in the presence of Fe (II), isopropanol, and Cr (VI) as the scavenger, the photocatalytic disinfection efficiency is almost the same as that without scavenger addition, which indicates that the role of H_2O_2, ·OH, and e^- can be ignored. However, the survival rate of *E. coli* K12 was 64% at 2 h in the presence of sodium oxalate which is much higher than that of no scavenger addition. This result indicates that the photogenerated h^+ plays the most important role in the photocatalytic bacterial inactivation process by omg-C_3N_4, which is consistent with the previous reports [21, 32, 33]. Therefore, the high bacterial inactivation efficiency of omg-C_3N_4 is due to high reaction opportunity with photogenerated h^+ but not the change of the band structure.

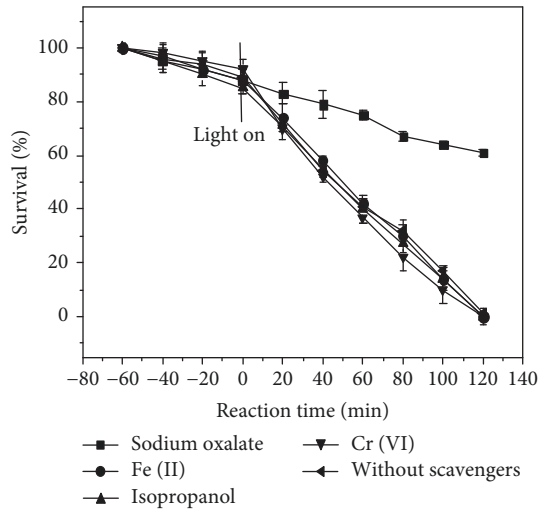

Figure 11: Photocatalytic bacterial inactivation against *E. coli* K-12 by omg-C_3N_4 with different scavenger addition under visible light irradiation.

4. Conclusions

In summary, ordered mesoporous g-C_3N_4 with a large surface area and a uniform pore size was synthesized with SBA-15 as the hard template. The as-prepared omg-C_3N_4

showed much enhanced photocatalytic inactivation efficiency for *E. coli* K12 under VL irradiation. The results of scavenger experiments suggested that the photogenerated hole plays an essential role in the bacterial inactivation process. As a proof of concept, this work demonstrates that the ordered mesoporous structures are particularly promising as host semiconductor scaffolds for the design of hybrid visible-light-driven photocatalysts for bacterial inactivation. Moreover, further functionalization by surface reaction or deposition is expected to produce a series of new g-C_3N_4-based materials for environmental water disinfection applications.

Data Availability

The data used to support the findings of this study are included within the manuscript.

Conflicts of Interest

The authors declare that they have no conflicts of interest.

Acknowledgments

This work was financially supported by the Natural Science Foundation of Fujian Province (2016J05042), the National Science Foundation of China (21607028), the New Century Talents Support Program of Fujian Province, and the Scientific Project of Putian Science and Technology Bureau (2016S1001, 2018ZP03, and 2018ZP07).

References

[1] N. J. Zinia and C. Kroeze, "Future trends in urbanization and coastal water pollution in the Bay of Bengal: the lived experience," *Environment, Development and Sustainability*, vol. 17, no. 3, pp. 531–546, 2015.

[2] L. E. D. Smith and G. Siciliano, "A comprehensive review of constraints to improved management of fertilizers in China and mitigation of diffuse water pollution from agriculture," *Agriculture, Ecosystems & Environment*, vol. 209, pp. 15–25, 2015.

[3] M. I. Uyaguari-Diaz, M. Chan, B. L. Chaban et al., "A comprehensive method for amplicon-based and metagenomic characterization of viruses, bacteria, and eukaryotes in freshwater samples," *Microbiome*, vol. 4, no. 1, p. 20, 2016.

[4] Q. Li, S. Mahendra, D. Y. Lyon et al., "Antimicrobial nanomaterials for water disinfection and microbial control: potential applications and implications," *Water Research*, vol. 42, no. 18, pp. 4591–4602, 2008.

[5] Y. Zhuang, H. Ren, J. Geng et al., "Inactivation of antibiotic resistance genes in municipal wastewater by chlorination, ultraviolet, and ozonation disinfection," *Environmental Science and Pollution Research*, vol. 22, no. 9, pp. 7037–7044, 2015.

[6] R. F. Lane, C. D. Adams, S. J. Randtke, and R. E. Carter Jr., "Chlorination and chloramination of bisphenol A, bisphenol F, and bisphenol A diglycidyl ether in drinking water," *Water Research*, vol. 79, pp. 68–78, 2015.

[7] T. Matsunaga, R. Tomoda, T. Nakajima, and H. Wake, "Photoelectrochemical sterilization of microbial cells by semiconductor powders," *FEMS Microbiology Letters*, vol. 29, no. 1-2, pp. 211–214, 1985.

[8] F. Chang, J. Zhang, Y. Xie et al., "Fabrication, characterization, and photocatalytic performance of exfoliated g-C_3N_4–TiO_2 hybrids," *Applied Surface Science*, vol. 311, pp. 574–581, 2014.

[9] F. Wu, X. Li, W. Liu, and S. Zhang, "Highly enhanced photocatalytic degradation of methylene blue over the indirect all-solid-state Z-scheme g-C_3N_4-RGO-TiO_2 nanoheterojunctions," *Applied Surface Science*, vol. 405, pp. 60–70, 2017.

[10] J. C. Yu, W. Ho, J. Yu, H. Yip, P. K. Wong, and J. Zhao, "Efficient visible-light-induced photocatalytic disinfection on sulfur-doped nanocrystalline titania," *Environmental Science & Technology*, vol. 39, no. 4, pp. 1175–1179, 2005.

[11] Y. Lan, C. Hu, X. Hu, and J. Qu, "Efficient destruction of pathogenic bacteria with AgBr/TiO_2, under visible light irradiation," *Applied Catalysis. B, Environmental*, vol. 73, no. 3-4, pp. 354–360, 2007.

[12] E. V. Skorb, L. I. Antonouskaya, N. A. Belyasova, D. G. Shchukin, H. Möhwald, and D. V. Sviridov, "Antibacterial activity of thin-film photocatalysts based on metal-modified TiO_2, and TiO_2 :In_2O_3, nanocomposite," *Applied Catalysis. B, Environmental*, vol. 84, no. 1-2, pp. 94–99, 2008.

[13] O. Seven, B. Dindar, S. Aydemir, D. Metin, M. A. Ozinel, and S. Icli, "Solar photocatalytic disinfection of a group of bacteria and fungi aqueous suspensions with TiO_2, ZnO and Sahara desert dust," *Journal of Photochemistry and Photobiology A: Chemistry*, vol. 165, no. 1-3, pp. 103–107, 2004.

[14] W. Wang, T. W. Ng, W. K. Ho et al., "$CdIn_2S_4$ microsphere as an efficient visible-light-driven photocatalyst for bacterial inactivation: synthesis, characterizations and photocatalytic inactivation mechanisms," *Applied Catalysis B: Environmental*, vol. 129, pp. 482–490, 2013.

[15] J. H. Hsieh, C. C. Chang, Y. K. Chang, and J. S. Cherng, "Photocatalytic and antibacterial properties of TaON-Ag nanocomposite thin films," *Thin Solid Films*, vol. 518, no. 24, pp. 7263–7266, 2010.

[16] K. S. Lakhi, D. H. Park, K. al-Bahily et al., "Mesoporous carbon nitrides: synthesis, functionalization, and applications," *Chemical Society Reviews*, vol. 46, no. 1, pp. 72–101, 2017.

[17] Y. Wang, X. Wang, and M. Antonietti, "Polymeric graphitic carbon nitride as a heterogeneous organocatalyst: from photochemistry to multipurpose catalysis to sustainable chemistry," *Angewandte Chemie International Edition*, vol. 51, no. 1, pp. 68–89, 2012.

[18] J. Huang, M. Antonietti, and J. Liu, "Bio-inspired carbon nitride mesoporous spheres for artificial photosynthesis: photocatalytic cofactor regeneration for sustainable enzymatic synthesis," *Journal of Materials Chemistry A*, vol. 2, no. 21, pp. 7686–7693, 2014.

[19] Y. Li, C. Zhang, D. Shuai, S. Naraginti, D. Wang, and W. Zhang, "Visible-light-driven photocatalytic inactivation of MS_2 by metal-free g-C_3N_4: virucidal performance and mechanism," *Water Research*, vol. 106, pp. 249–258, 2016.

[20] H. Zhao, H. Yu, X. Quan et al., "Fabrication of atomic single layer graphitic-C_3N_4 and its high performance of photocatalytic disinfection under visible light irradiation," *Applied Catalysis B: Environmental*, vol. 152-153, no. 25, pp. 46–50, 2014.

[21] J. Huang, W. Ho, and X. Wang, "Metal-free disinfection effects induced by graphitic carbon nitride polymers under visible

light illumination," *Chemical Communications*, vol. 50, no. 33, pp. 4338–4340, 2014.

[22] J. Zhang, F. Guo, and X. Wang, "An optimized and general synthetic strategy for fabrication of polymeric carbon nitride nanoarchitectures," *Advanced Functional Materials*, vol. 23, no. 23, pp. 3008–3014, 2013.

[23] Z. Zhao, Y. Dai, J. Lin, and G. Wang, "Highly-ordered mesoporous carbon nitride with ultrahigh surface area and pore volume as a superior dehydrogenation catalyst," *Chemistry of Materials*, vol. 26, no. 10, pp. 3151–3161, 2014.

[24] Y. Guo, Q. Liu, Z. Li, Z. Zhang, and X. Fang, "Enhanced photocatalytic hydrogen evolution performance of mesoporous graphitic carbon nitride co-doped with potassium and iodine," *Applied Catalysis B: Environmental*, vol. 221, pp. 362–370, 2018.

[25] X. Chen, Y. S. Jun, K. Takanabe et al., "Ordered mesoporous SBA-15 type graphitic carbon nitride: a semiconductor host structure for photocatalytic hydrogen evolution with visible light," *Chemistry of Materials*, vol. 21, no. 18, pp. 4093–4095, 2009.

[26] J. Zhang, T. Cai, H. Li, and H. Zhao, "Synthesis g-C_3N_4 of high specific surface area by precursor pretreatment strategy with SBA-15 as a template and their photocatalytic activity toward degradation of rhodamine B," *Phosphorus, Sulfur, and Silicon and the Related Elements*, vol. 194, no. 3, pp. 229–235, 2019.

[27] D. Zhao, J. Feng, Q. Huo et al., "Triblock copolymer syntheses of mesoporous silica with periodic 50 to 300 angstrom pores," *Science*, vol. 279, no. 5350, pp. 548–552, 1998.

[28] L. S. Zhang, K. H. Wong, H. Y. Yip et al., "Effective photocatalytic disinfection of *E. coli* K-12 using AgBr-Ag-Bi_2WO_6 nanojunction system irradiated by visible light: the role of diffusing hydroxyl radicals," *Environmental Science & Technology*, vol. 44, no. 4, pp. 1392–1398, 2010.

[29] T. Wang, X. Meng, P. Li et al., "Photoreduction of CO_2 over the well-crystallized ordered mesoporous TiO_2 with the confined space effect," *Nano Energy*, vol. 9, pp. 50–60, 2014.

[30] F. Dong, H. Liu, W. K. Ho, M. Fu, and Z. Wu, "$(NH4)_2CO_3$ mediated hydrothermal synthesis of N-doped $(BiO)_2CO_3$ hollow nanoplates microspheres as high-performance and durable visible light photocatalyst for air cleaning," *Chemical Engineering Journal*, vol. 214, pp. 198–207, 2013.

[31] S. Hwang, S. Lee, and J. S. Yu, "Template-directed synthesis of highly ordered nanoporous graphitic carbon nitride through polymerization of cyanamide," *Applied Surface Science*, vol. 253, no. 13, pp. 5656–5659, 2007.

[32] J. H. Huang, W. T. Lin, L. Y. Xie, and J. Q. Chen, "Construction of graphitic carbon nitride-bismuth oxyiodide layered heterostructures and their photocatalytic antibacterial performance," *Huan Jing Ke Xue= Huanjing Kexue*, vol. 38, no. 9, pp. 3979–3986, 2017.

[33] W. Wang, J. C. Yu, D. Xia, P. K. Wong, and Y. Li, "Graphene and g-C_3N_4 nanosheets cowrapped elemental α-sulfur as a novel metal-free heterojunction photocatalyst for bacterial inactivation under visible-light," *Environmental Science & Technology*, vol. 47, no. 15, pp. 8724–8732, 2013.